Polarization and plasmons in hot photoexcited graphene

A. Freddie Page, Joachim M. Hamm, and Ortwin Hess*
Blackett Laboratory, Department of Physics, Imperial College London, London SW7 2AZ, United Kingdom

(Received 17 August 2017; revised manuscript received 15 January 2018; published 29 January 2018)

We present a robust and exact method for calculating the polarization function and plasmon dispersion of graphene, for an arbitrary (isotropic) nonequilibrium carrier distribution, within the random phase approximation. This is demonstrated for a range of carrier distributions, including hot-carrier distributions which occur within the femtoseconds following photoexcitation. We show that qualitatively different behavior from the equilibrium case can occur. As the polarization function determines dynamic screening, its calculation will be essential to quantifying carrier-carrier scattering channels for graphene far from equilibrium.

DOI: 10.1103/PhysRevB.97.045428

I. INTRODUCTION

Graphene stands out among other two-dimensional materials due to the presence of Dirac points in its band structure, with an approximately linear electronic dispersion and a vanishing band gap. One of the most important consequences of this band structure is the possibility for low-energetic electron/hole pairs to interact with plasmons via plasmon absorption or emission; this is excluded in band-gap materials where the energy of plasmons is typically much smaller than that of single-particle excitations [1,2].

When graphene is excited with a femtosecond optical pulse, high-energetic electron/hole pairs are generated far from the Fermi edge. Carrier-carrier and carrier-plasmon scattering will cause a rapid redistribution of the energy in the carrier system, on a 10–100 fs scale [3], first bringing the plasma into a two-component inverted quasiequilibrium and then into a state of a high-temperature carrier equilibrium [4–7]. Following the equilibration in the carrier system, the plasma will equilibrate with the phonon system, albeit on longer time scales, as carrier-phonon scattering is typically at least one order of magnitude slower than carrier-carrier scattering [8–10]. Excitation and relaxation processes are illustrated in Fig. 1. During this relaxation process, the scattering of carriers and their interaction with plasmons are mediated by the screened Coulomb potential $V_{\mathbf{q}}^{\mathrm{eff}}(q,\omega) = V_q/\varepsilon(q,\omega)$, where V_q is the bare Coulomb potential and $\varepsilon(q,\omega)$ the dynamic dielectric function, which in turn depends on the dynamically evolving nonequilibrium distribution of carriers. Therefore, when evaluating the scattering probabilities associated with plasmas far from equilibrium, it is not sufficient to assume equilibrium dielectric functions, but instead one needs to evaluate the nonequilibrium dielectric function of the plasma associated with the momentary carrier distribution. For graphene this was, to the best of our knowledge, first pointed out in Ref. [11], where the dielectric function is evaluated for a two-component plasma in a quasiequilibrium to describe the dynamic screening of Auger processes, using a procedure described by Maldague [12,13]. At the same level, the plasmon dispersion, defined by the zeros of the dielectric function, $\varepsilon(q,\omega) = 0$, is also functionally dependent on the carrier distribution. A recent experimental study has shown the plasmon response of graphene can be activated by pulsed optical excitation, due to the increase in Drude weight associated with generated nonequilibrium carriers [14]. It has been shown in Ref. [15] that photoexcitation beyond the Dirac cone can give support to plasmons with anisotropic dispersion relations. In a previous work [16], we have solved the plasmon dispersion for photoinverted graphene and found that it differs fundamentally from the equilibrium dispersion, as the phase space for net stimulated emission grows and plasmons can become amplified [17]. However, the method used therein to calculate the plasmon dispersion is only applicable to a two-component plasma in quasiequilibrium and at temperatures much smaller than the chemical potentials ($k_{\mathrm{B}}T \ll \mu_{\mathrm{e}},\mu_{\mathrm{h}}$). Crucially, it does not accommodate for more general carrier occupations, such as the presence of high-energetic carriers that are generated during optical excitation.

In this work, we show how to efficiently calculate the polarization function (and hence the dielectric function), and plasmon dispersion of graphene for arbitrary isotropic nonequilibrium carrier distributions within the random phase approximation (RPA). While the formalism can be extended, we further assume the electronic dispersion of graphene to be a gapless Dirac cone, i.e., as described by the massless Dirac fermion (MDF) model. Crucially, the method presented here fully accommodates the conditions encountered during pulsed photoexcitation: it is applicable to an electron/hole plasma at high temperatures ($k_{\mathrm{B}}T \gg \mu_{\mathrm{e}},\mu_{\mathrm{h}}$) and allows us to incorporate the influence of high-energetic carriers.

This paper is structured as follows: First we present the general theory that allows the polarization function for isotropic nonequilibrium carrier distributions to be efficiently evaluated on the basis of zero-temperature equilibrium polarization functions. Next, to determine the complex-frequency plasmon dispersion, we present a contour-integration method that remains valid at high temperatures and when taking into account the photogenerated high-energetic carriers characteristic of a plasma far from equilibrium. To demonstrate the versatility of the method we calculate the energy-loss

*o.hess@imperial.ac.uk

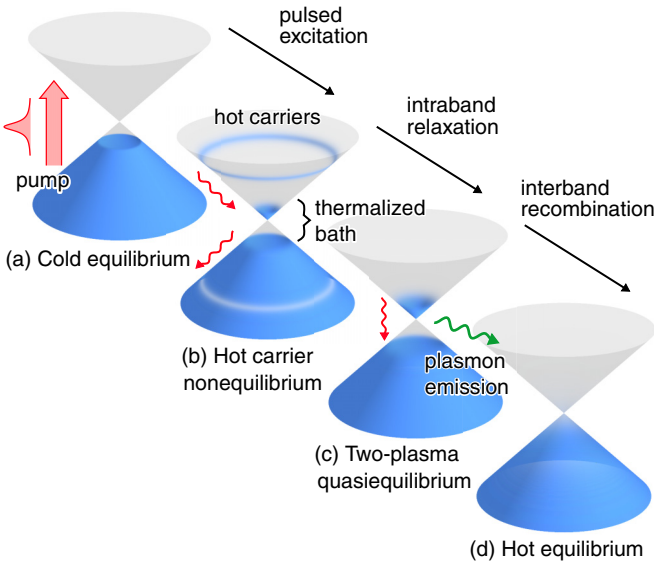

FIG. 1. Highly energetic electron-hole pairs (hot carriers) are excited in graphene by a pulsed femtosecond beam. These carriers then relax by intraband processes on a 10–100 fs time scale and pool at the Dirac point approaching a thermalized two-component quasiequilibrium distribution, before relaxing to a warm carrier equilibrium where the electrons are in thermal equilibrium, though at a higher temperature than the phonons and ambient surroundings. Such varying electronic configurations determine the energy scale and character of the dynamic screening and the supported plasmon modes on the sheet, as well as whether net stimulated emission of plasmons is possible.

function and plasmon dispersion for three different cases: a high-temperature equilibrium, a high-temperature inverted two-component quasiequilibrium, and a nonequilibrium case that combines a hot quasiequilibrium bath with a distribution of photoexcited high-energy carriers.

II. THEORY

A. Nonequilibrium polarization function

The Coulomb interaction of a pair of electrons in graphene is effectively screened by the collective of electrons (the MDF plasma) according to $V_{\mathbf{q}}^{\mathrm{eff}} = V_q/\varepsilon(\mathbf{q},\omega)$, where $V_q = e^2/(2\bar{\varepsilon}\varepsilon_0 q)$ is the 2D Fourier transform of the Coulomb potential, for excitations with frequency ω and in-plane wave vector $\mathbf{q}$, and where $\varepsilon(\mathbf{q},\omega)$ is the dynamic dielectric (or screening) function. It can be expressed, within RPA, as [18]

$$\varepsilon(\mathbf{q},\omega) = 1 - V_q \Pi(\mathbf{q},\omega), \tag{1}$$

introducing $\Pi(\mathbf{q},\omega)$, the polarization function, given by the bare bubble diagram. Importantly, the poles of the effective Coulomb potential, $\varepsilon(\mathbf{q},\omega) = 0$, signify collective plasmon excitations, freely propagating charge density waves that transport energy and momentum [1]. It has been shown that despite an interaction constant larger than 1, the MDF plasma of graphene behaves like a weakly interacting electron gas and application of the RPA is well justified [19].

The polarization function which relates to the (nonlocal) sheet conductivity of graphene, $\sigma_s(\mathbf{q},\omega) = ie^2\omega/q^2\,\Pi(\mathbf{q},\omega)$ [18], is calculated using the Lindhard equation [20,21],

$$\Pi[n](\mathbf{q},\omega) = \frac{g}{A}\sum_{\mathbf{k},s,s'} M^{ss'}_{\mathbf{k},\mathbf{k}+\mathbf{q}} \frac{n\left(\epsilon^s_{\mathbf{k}}\right) - n\left(\epsilon^{s'}_{\mathbf{k}+\mathbf{q}}\right)}{\epsilon^s_{\mathbf{k}} - \epsilon^{s'}_{\mathbf{k}+\mathbf{q}} + \hbar(\omega + i\eta)}, \tag{2}$$

in the limit as $\eta \to 0^+$. The equation above introduces the in-plane electron wave vector $\mathbf{k}$, indices $s,s' = \pm$ labeling the conduction and valence band, electron degeneracy g, and sheet area A. Further, for graphene in the MDF approximation, the matrix element is given by $M^{ss'}_{\mathbf{k},\mathbf{k}'} = (1 + ss'\cos\theta_{\mathbf{k},\mathbf{k}'})/2$ and electronic dispersion $\epsilon^s_{\mathbf{k}} = s\hbar v_{\mathrm{F}}|\mathbf{k}|$, with Fermi velocity $v_{\mathrm{F}} \approx c/300$. In the scope of this work, we assume nonequilibrium carrier distributions that are functions of energy, $n(\epsilon^s_{\mathbf{k}})$, and that the carrier energy is isotropic in $\mathbf{k}$ space, i.e., $\epsilon^s_{\mathbf{k}} = \epsilon^s_k$. It follows that the response will thereby be isotropic, so herein we drop the vector character of $\mathbf{q}$ in favor of q.

Fundamentally, the equation for the polarization and dielectric functions remain valid in nonequilibrium as long as pair excitations are not too highly damped, so that it is possible to define nonequilibrium distribution functions, $n(\epsilon^s_k)$ [22]. That is, if the relaxation rates of the distributions are long compared to the oscillation time scales of the excitations, one can neglect non-Markovian contributions [23]. Experimental measurements of the ultrafast carrier dynamics of optically excited carriers at 0.8 eV give a fastest relaxation time scale of 10–150 fs, followed by slower cooling and recombination on a 150 fs to 15 ps time scale [4,24]. At an oscillation period of 5.2 fs, such carriers would be well described by a Markovian model, which permits the use of the model presented herein in cases of equilibrium and two-component quasiequilibrium, and for hot photoexcited distributions.

A general expression for the nonequilibrium polarization function can be constructed based on the equilibrium polarization [Eq. (2)], as first demonstrated in Ref. [16]. In the following we briefly present this result, before detailing how the result is applied to both screening and plasmons. First, we make use of the delta function identity,

$$\Pi[n] = \Pi\left[\int_{-\infty}^{\infty} d\epsilon\, n(\epsilon)\delta(\epsilon - \circ)\right], \tag{3}$$

where "$\circ$" is the dummy variable which the outer Π functional operates over. The (q,ω) dependence is omitted for clarity. Then, as Eq. (2) is a linear functional of the carrier distribution, we are able to swap the order of the integration and the functional, so that only the delta function remains inside the functional,

$$\Pi[n] = \int_{-\infty}^{\infty} d\epsilon\, \Pi[\delta(\epsilon - \circ)]n(\epsilon). \tag{4}$$

The delta function can be expressed as the derivative of a zero-temperature Fermi function, i.e., a Heaviside step function, the polarization function of which is well known [20,21,25]. This allows the polarization function to be expressed as an integral transform of the carrier density,

$$\Pi[n] = \int_{-\infty}^{\infty} d\epsilon \frac{\partial \Pi^{T=0}_{\mu=\epsilon}}{\partial\epsilon} n(\epsilon). \tag{5}$$

The integral can be split into contributions from electrons and holes by introducing carrier distribution functions, n_{e} and n_{h},

where

$$n(\epsilon) = n_e(\epsilon)\theta(\epsilon) + [1 - n_h(-\epsilon)]\theta(-\epsilon), \tag{6}$$

with the Heaviside step function $\theta(\epsilon)$ separating contributions from the conduction and valence band. The polarization function then takes form as a sum of the polarization function of intrinsic graphene and contributions from electrons and holes,

$$\Pi[n] = \Pi^{T=0}_{\mu=0} + \int_0^\infty d\epsilon\, [\Pi'(\epsilon)n_e(\epsilon) + \Pi'(-\epsilon)n_h(\epsilon)], \tag{7}$$

with $\Pi'(\epsilon) = \frac{\partial}{\partial\epsilon}\Pi^{T=0}_{\mu=\epsilon}$ for brevity. For systems with particle-hole symmetry, i.e., $\Pi'(\epsilon) = \Pi'(-\epsilon)$, such as MDF graphene, Eq. (7) can be written in terms of the joint occupation $n_e + n_h$. This can be further split into a sum, $n_e + n_h = \sum_i n_i$, whose contributions to the polarization function can be evaluated separately, due to linearity, i.e.,

$$\Pi[n] = \Pi^{T=0}_{\mu=0} + \sum_i \int_0^\infty d\epsilon\, \Pi'(\epsilon)n_i(\epsilon). \tag{8}$$

This is a general result that holds for any material with isotropic band structure and carrier distributions, within the RPA, not just graphene.

For graphene in the MDF approximation, the intrinsic contribution is [27]

$$\Pi^{T=0}_{\mu=0} = \frac{g}{8\pi\hbar^2 v_F^2}\frac{-i\pi(u-v)^2}{4\sqrt{u}\sqrt{v}}, \tag{9}$$

where new coordinates $u = \hbar(\omega + v_F q)/2$ and $v = \hbar(\omega - v_F q)/2$ along the axes parallel and perpendicular to the Dirac cone have been introduced. These coordinates are particularly convenient to highlight the position of branch points in the polarization function. For graphene in the MDF model, the integral kernel is particle/hole symmetric, $\Pi'(\epsilon) = \Pi'(-\epsilon)$, and takes the simple form [16]

$$\Pi'(\epsilon) = \frac{g}{8\pi\hbar^2 v_F^2}[\tilde{\Pi}'_+(\epsilon) + \tilde{\Pi}'_-(\epsilon)], \tag{10a}$$

$$\tilde{\Pi}'_\pm(\epsilon) = \frac{2i\sqrt{\pm i(\epsilon \mp u)}\sqrt{\pm i(\epsilon \mp v)} \pm 2\epsilon}{\sqrt{u}\sqrt{v}} - 2. \tag{10b}$$

There are four branch points in Eq. (10) coming from the square-root terms, $\epsilon = \pm u$ and $\epsilon = \pm v$, shown as blue "$*$" in the complex-ϵ plane in Fig. 2(a), which lie on the real axis for real values of (q,ω). The branch cuts in Eq. (10) have been positioned vertically (see Appendix A); the integration can therefore be carried out directly on the real-ϵ axis (green line), without the infinitesimal shift prescribed by Eq. (2).

Equation (8), along with the definitions in Eqs. (9) and (10), is all that is needed to evaluate the nonequilibrium polarization function for real-valued arguments (q,ω). As such it is sufficient when calculating the screening function and energy-loss spectrum (see Sec. III A). However, when tracing the plasmon pole $\varepsilon(q,\omega) = 0$ for real-valued wave vectors q, the plasmon frequency becomes complex [25] and the branch points in Fig. 2 are no longer situated on the real-ϵ axis. In this circumstance the branch points may cut through the integration contour, as shown in Fig. 2(b), and the value of the integral cannot be uniquely determined. The following section deals with the proper treatment of the integral in this situation.

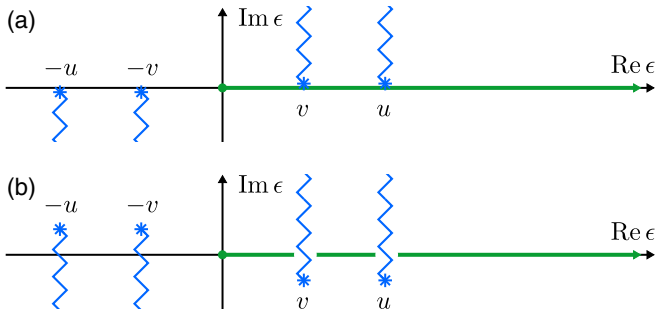

FIG. 2. Complex-ϵ plane diagram for the integration in Eq. (8). The integration path is shown as the green line along the real axis. Branch points of the integration kernel [Eq. (10)] are shown as blue "$*$" at $\epsilon = \pm u, \pm v$. Branch cuts stem from the branch points and are set vertically such that in (a) the function evaluates as if an infinitesimal positive imaginary part was added to u and v, when q and ω are real. In (b) ω is complex, so u and v have acquired finite imaginary parts, causing the branch points to pierce the integration contour.

B. Nonequilibrium plasmon dispersion relations

Plasmons exist at frequencies where there is a pole in the effective Coulomb potential, i.e., for the zeros of the dielectric function [Eq. (1)], i.e.,

$$\varepsilon(q,\omega) = 0. \tag{11}$$

The dielectric function is complex valued in regions where there is Landau damping or electron-hole recombination, so it follows that for a real wave vector, the roots themselves are at complex frequencies,

$$\omega = \omega_{pl} - i\gamma_{pl}, \tag{12}$$

where the real part is proportional to the energy of the plasmon, $\hbar\omega_{pl}$, and the imaginary part is proportional to the net stimulated absorption rate of the plasmon number density, $2\gamma_{pl} = \gamma_{stim} = \gamma_{abs} - \gamma_{emit}$. Commonly, an approximation to the root is found by solving

$$\mathrm{Re}\,\varepsilon(q,\omega_{pl}) = 0, \tag{13}$$

for a real frequency, $\omega_{pl}(q)$, given a real q. The imaginary part is then evaluated by taking a first-order Taylor expansion about ω_{pl}, perturbing by $-i\gamma_{pl}$, and solving, which leads to [20,28]

$$\gamma_{pl} = \frac{\mathrm{Im}\,\varepsilon(q,\omega_{pl})}{\mathrm{Re}\,\frac{\partial\varepsilon}{\partial\omega}(q,\omega_{pl})}. \tag{14}$$

This approximation holds when the solved decay rate is small with respect to the frequency, $\gamma_{pl} \ll \omega_{pl}$. In this approximation however, as was shown in [16], the decay rate grows without bounds for increasing q, and deviations from the exact complex solution are clearly visible in both real and imaginary parts, as well as a failure to produce correct emission spectra in the photoinverted case. This section will detail how complex frequency plasmon dispersion relations can be found for graphene with arbitrary carrier configurations.

Figure 2 shows the integration of Eq. (8) in the case of real-valued frequencies; there the integration contour is a straight line along the real axis from zero to infinity. When the frequencies become complex, the branch points detach from

the real axis and may cut through the integration contour, in which case the polarization function evaluates incorrectly as the integral cannot be uniquely defined. Evaluation of Eq. (11) for complex frequencies thus requires a deformation of the integration contour and the branch cuts such that both vary continuously with increasing wave vector q and that neither crosses the other in complex-ϵ space.

In general, an integral is independent of its integration contour; any two paths with the same end points that can be continuously deformed from one to the other will yield the same result, as long as no singularities are crossed during the deformation. Applying this principle to the polarization function, the contour of integration, in Eq. (8), can be altered by taking it off the real axis to allow the branch points to move in a region below the real axis.

In addition to branch points, the other singularities that may appear in the integrand are the poles of the carrier distribution function $n(\epsilon)$. The positions of these poles are fixed in the complex-ϵ plane, independent of the dynamic variables (q,ω). As with branch points, the integration contour must not pass over poles without being corrected for. The Fermi function, $n(\epsilon) = \{1 + \exp[(\epsilon - \mu)/T]\}^{-1}$, for example, has its poles at the complex fermionic Matsubara frequencies, $\epsilon^{(n)} = \mu + i(2n+1)\pi T$ with residue $-T$. If the integration contour passes over a pole, at $\epsilon_\times$, the integral will gain a contribution due to the residue of the pole, i.e., the integral of a closed contour encircling that pole, $\mathcal{C}_\times$. For a pole in the carrier distribution function this contribution is

$$\oint_{\mathcal{C}_\times} d\epsilon\ \Pi'(\epsilon) n(\epsilon) = 2\pi i \Pi'(\epsilon_\times) \operatorname{Res}_{\epsilon_\times} n(\epsilon). \tag{15}$$

Therefore, the integration contour in Eq. (8) can be altered to pass over poles as long as the contributions of the residues are subtracted.

Apart from the poles of the carrier distribution, which are explicitly accounted for by Eq. (15), the prescription for calculation plasmon dispersion curves is that the integration contour must not be crossed by singularities as they move through ϵ space, and that the contour is to be deformed to enforce this. It is useful here to break the integral into two parts, and calculate the $\tilde{\Pi}'_+(\epsilon)$ and $\tilde{\Pi}'_-(\epsilon)$ contributions to the integration kernel in Eq. (10a) separately. This will allow a different contour to be used in each part, and particularly will separate the branch point singularities, so that only one pair has to be considered in each integral. For such evaluation, the favorable choice of branch cuts changes, as illustrated in Fig. 3 (see Appendix A), and Eq. (10b) is replaced by

$$\tilde{\Pi}'_+(\epsilon) = \frac{-2\sqrt{\epsilon-u}\sqrt{\epsilon-v} + 2\epsilon}{\sqrt{u}\sqrt{v}} - 2, \tag{16a}$$

$$\tilde{\Pi}'_-(\epsilon) = \frac{-2i\sqrt{i(\epsilon+u)}\sqrt{i(\epsilon+v)} - 2\epsilon}{\sqrt{u}\sqrt{v}} - 2. \tag{16b}$$

For the first equation, this keeps the branch cut compact, whereas the second equation orients the cuts at $-u$ and $-v$ vertically upwards (blue zigzag lines, as shown in Fig. 3). The $\tilde{\Pi}'_-$ kernel is integrated along the real line but the $\tilde{\Pi}'_+$ contribution follows a contour that, starting from zero, cups the branch points u and v from underneath, and corrects for any poles that would not have otherwise been included by a contour along the real axis.

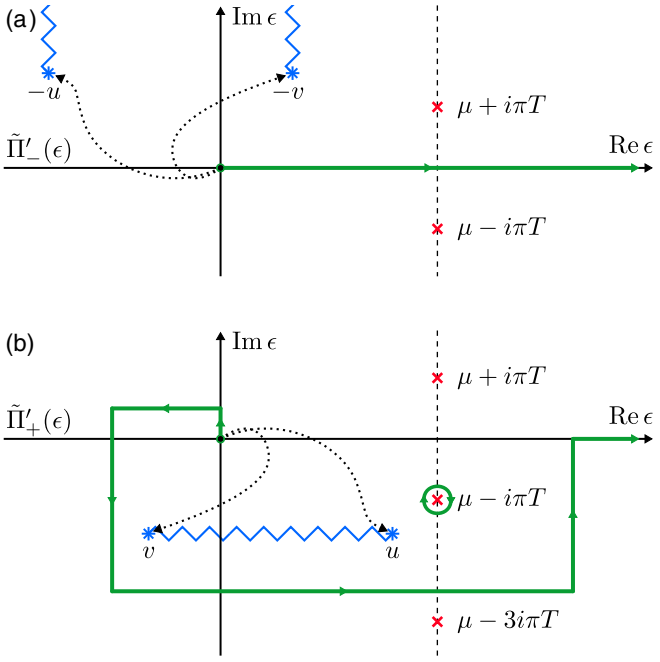

FIG. 3. Complex contour integration for solving plasmon dispersion relations. (a) and (b) show the integration contour (green line) of $\int d\epsilon \tilde{\Pi}'_\pm(\epsilon) n(\epsilon)$. Poles are shown as red "×", i.e., here for a Fermi distribution. Branch points are represented as blue "∗". The black dotted line illustrates how the branch points move as the solutions to $\varepsilon(q,\omega) = 0$ evolve with increasing q. (a) integrates the $\tilde{\Pi}'_-$ kernel, over the positive real line, while (b) integrates $\tilde{\Pi}'_+$ over a contour that avoids being crossed by the moving branch points. One of the contained poles has been circled with a clockwise integration to indicate that the contribution of this pole must be subtracted, with the contour having passed over it.

Given a form for the polarization function, it still remains to find a solution to Eq. (11). For the complex frequency plasmon solutions, $\varepsilon(q,\omega)$ takes q as a real parameter, and a complex-ω is found for each q which solves Eq. (11). When treated as described herein, the dielectric function is well behaved as a function of a complex-ω in the vicinity of solutions. As such, standard complex root finding methods, e.g., Newton's method, that are available in numeric software packages can be used. The starting value for the root finding method, in the first instance, can be the solution to an equivalent system with a Drude conductivity, as will be described in Sec. III B, and subsequently a complex frequency solution for a nearby q that has been previously solved for should be used.

Examples of plasmon dispersion relations calculated in this way are presented in the next section.

III. HIGH-TEMPERATURE EQUILIBRIUM AND QUASIEQUILIBRIUM

A. Energy-loss function and plasmon dispersion

To demonstrate the contour integration method, we first evaluate the complex frequency plasmon dispersion, $\omega_{\mathrm{pl}} - i\gamma_{\mathrm{pl}}$, together with the energy-loss function, $S = \operatorname{Im} \varepsilon(q,\omega)^{-1}$,

for both equilibrium and two-component quasiequilibrium, at finite temperatures T (given in units of energy). In both cases the carrier distribution functions for each band (n_e, n_h) are Fermi functions, $n_{e/h} = \{1 + \exp[(\epsilon - \mu_{e/h})/T]\}^{-1}$. The energy-loss function is shown in Fig. 4, alongside the corresponding complex frequency plasmon dispersion curves. Panels (a)–(d) are for equilibrium graphene, where there is a single Fermi level, i.e., the chemical potentials of each carrier species are of equal magnitude but opposite sign ($\mu_e = -\mu_h = \mu$). Panel (a) is for zero temperature. Here the Fermi edge is sharp and Landau damping is confined to regions permitted by energy and momentum conservation. The energy-loss function S is finite in these regions and zero in the so-called quasi-loss-free regions, the triangular regions in the plot. The complex frequency plasmon dispersion (first solved at zero-temperature equilibrium in [25]) is shown here as a green line. The energy-loss function is resonant about the plasmon dispersion curve, and is broader where the plasmon loss γ_{pl} is larger and sharper when it is small. The solution of the plasmon dispersion curve continues over the Dirac cone line, $\omega = v_F q$, into the intraband region. Notably this is not reflected in the energy-loss function as the plasmon curve has moved onto a different branch of the energy-loss function [26]. Figures 4(b)–4(d) show what happens to the plasmon dispersion and the energy-loss function as temperature is increased. The energy-loss function in this equilibrium case is in agreement with [29]. In the band, the Fermi edge stops being sharply defined and has a spread for finite temperatures. This results in the energy-loss function not being confined to well-defined regions, becoming finite everywhere. Again the energy-loss function is resonant about the plasmon dispersion, and this is more pronounced in regions of low loss, where the resonance is sharpest. The plasmon dispersion curves themselves become steeper as T is increased, remaining in the interband region for a wider range of wave vectors.

Figures 4(e)–4(h) account for the case of a two-component quasiequilibrium of excited intrinsic graphene. In this case, each band has its own Fermi level, and here ($\mu_e = \mu_h = \mu$). Panels (a)–(d) were scaled by the energy difference between the Dirac point and the Fermi level, μ, whereas panels (e)–(h) are scaled to the energy difference between the two Fermi levels, 2μ, as was the convention in [16]. With a population of electrons in the conduction band sitting above a population of holes in the valence band, recombination of electron-hole pairs by stimulated emission of plasmons becomes possible. At zero temperature, as in Fig. 4(e), this manifests as the energy-loss function being negative, indicating gain (red on the plot) in the interband region for energies less than 2μ. For frequencies above this, stimulated emission is no longer possible, and plasmons at these frequencies are absorbed by Landau damping (blue areas). At finite temperatures, where the Fermi edge is not sharply defined, phase space for stimulated emission at frequencies above 2μ and for absorption at frequencies below is allowed for. The net rate of stimulated emission/absorption however remains sharply defined at $\hbar\omega = 2\mu$, as reflected in panels (f)–(h). This is also despite the plasmon curves steepening and growing as they did in the equilibrium case, and hence dispersion curves for high temperatures having gain in a comparably narrow wave vector range.

The manner in which the curves for equilibrium and two-component quasiequilibrium scale with temperature is similar in both cases. In fact, for the highest temperature shown for each case, Fig. 4, panels (d) and (h), the dispersion curves and loss functions are almost identical. At high temperatures, it is indeed the temperature that is responsible for the scale of the features of the plasmon dispersion and energy-loss function, whereas at low temperatures, it is the chemical potentials that determine the scale and features such as inversion. In the next section, we shall introduce a scaling factor that generalizes for arbitrary carrier distributions in order to more clearly show how the behavior of plasmons changes depending on the carrier distribution.

B. Drude weight scaling

For regimes where temperature is much greater than the chemical potentials, the distribution function and hence polarization function is, in relative terms, insensitive to changes in either chemical potential. This is the regime of thermoplasma polaritons, where the loss function and plasmon dispersion scale linearly with temperature [30]. In contrast, for low temperatures, the plasmon dispersion scales primarily with the chemical potentials.

The Drude weight, defined as

$$D = \lim_{\omega\to 0} \omega \,\mathrm{Im}\,\sigma_s(0,\omega), \tag{17}$$

can be used as a scaling parameter for the plasmons. We introduce a derived frequency, ω_D, which later in this section we shall plot plasmon dispersion curves in relation to:

$$\omega_D = \frac{Z_0}{\alpha_0 g} D, \tag{18}$$

where α_0 is the fine-structure constant and Z_0 is the impedance of free space. To derive an expression for the Drude weight for a nonequilibrium distribution in RPA, it suffices to use an expression for the intraband surface conductivity in the local limit ($q \to 0$), given as [31]

$$\sigma_{intra}(0,\omega) = -\frac{ie^2 g}{4\pi\hbar^2\omega} \sum_i \int_0^\infty d\epsilon\, \epsilon \frac{\partial n_i}{\partial \epsilon}, \tag{19}$$

or more simply as

$$Z_0\sigma_{intra}(0,\omega) = i\alpha_0 g \frac{\omega_D}{\omega}, \tag{20}$$

where the integral term is equal to the Drude weight frequency (after integration by parts),

$$\hbar\omega_D = \sum_i \int_0^\infty d\epsilon\, n_i(\epsilon). \tag{21}$$

Substituting this into the solution for plasmons on a conducting sheet, $1 + icqZ_0\sigma_s(\omega)/(2\bar{\varepsilon}\omega) = 0$, returns the familiar square-root plasmon dispersion approximation,

$$\frac{\omega}{\omega_D} = \sqrt{\frac{g\alpha_0}{2\bar{\varepsilon}}}\sqrt{\frac{cq}{\omega_D}}, \tag{22}$$

or even more compactly as $\tilde{\omega} = \sqrt{2\alpha_g \tilde{q}}$ for $\tilde{\omega} = \omega/\omega_D$, $\tilde{q} = v_F q/\omega_D$, and $\alpha_g = g\alpha_0 c/(4\bar{\varepsilon} v_F)$, which is the long-wavelength limit for equilibrium distributions at zero [20,21,32] and finite

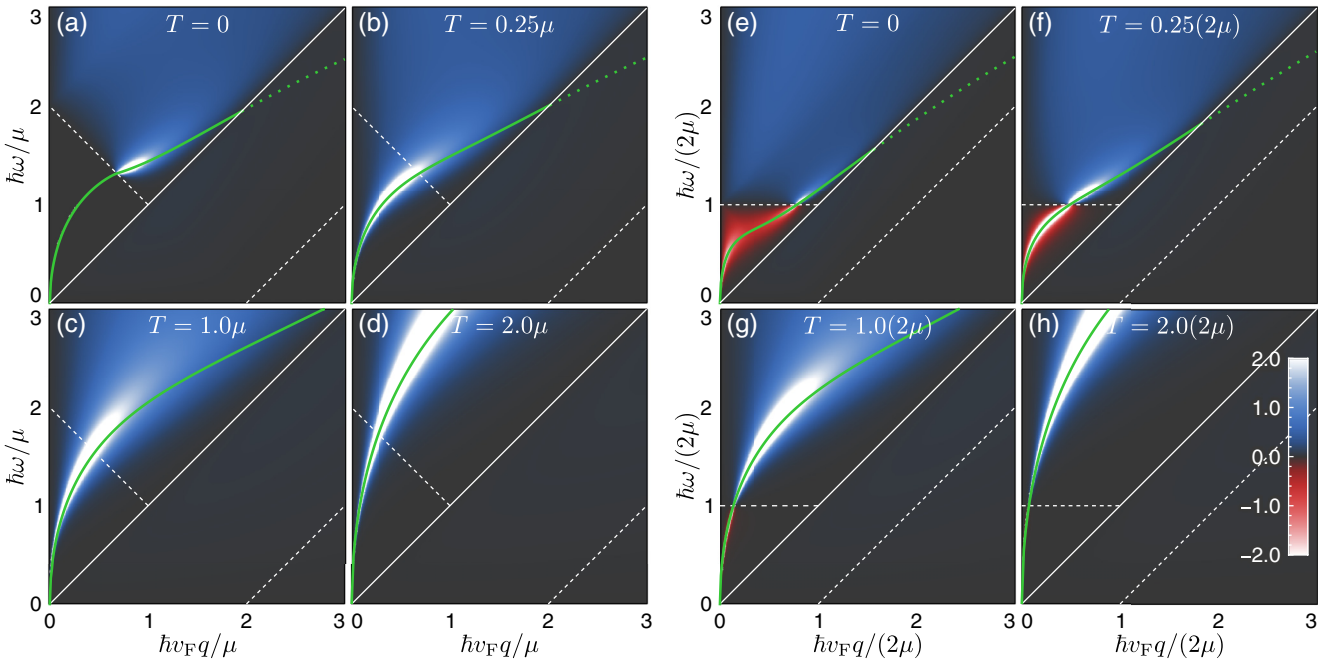

FIG. 4. Energy-loss function, $S = -\operatorname{Im}\varepsilon(q,\omega)^{-1}$, over a range of temperatures. The solid white diagonal line is the Fermi velocity, whereas the dotted lines are the boundaries of regions of Landau damping at zero temperature. Complex frequency plasmon dispersion curves are plotted as green lines over each plot (q, $\operatorname{Re}\omega_{\rm pl}(q)$). Panels (a)–(d): Equilibrium graphene for temperatures in the range $[0,2\mu]$. Panels (e)–(h): Two-component plasma in quasiequilibrium, following photoexcitation, with temperatures in the range $[0,4\mu]$. The inversion line at $\hbar\omega = 2\mu$ separates regions of interband spontaneous emission (gain) and absorption (loss); in these regions, the loss function is negative and is shown in red.

[29,33] temperature. Thus, when the frequency and wave vector are scaled by the Drude weight, the local limit of the plasmon dispersion is independent of the carrier distribution. We shall show later in this section that scaling by the Drude weight is indeed useful to identify general behavior when calculating the fully nonlocal complex-frequency plasmon dispersion.

The Drude weight in Eq. (21) is linear in carrier distribution, n, and therefore can be calculated for each contribution independently and summed for the total Drude weight. For a Fermi distribution in a single band, $n = \{1 + \exp[(\epsilon - \mu)/T]\}^{-1}$, the contribution to the Drude weight takes the form

$$\hbar\omega_{\rm D} \to T\ln(1 + e^{\mu/T}), \tag{23}$$

which in the limit where the chemical potential dominates, i.e., $\mu \gg T$, is purely $\hbar\omega_{\rm D} \to \mu$, and in the temperature-dominated regime, $T \gg \mu$, becomes $\hbar\omega_{\rm D} \to T\ln 2$.

For equilibrium graphene, the electron and hole chemical potentials are equal and opposite, $\mu_{\rm e} = -\mu_{\rm h} = \mu$. The sum of both contributions to the Drude weight, $\hbar\omega_{\rm D} = T\ln[(1 + e^{\mu_{\rm e}/T})(1 + e^{\mu_{\rm h}/T})]$, then becomes equivalent to the form, $2T\ln[2\cosh(\mu/2T)]$, as appears in Ref. [33].

Figure 5 shows complex-frequency RPA nonlocal plasmon dispersion curves scaled to the Drude weight $\omega_{\rm D}$. This figure is for graphene in equilibrium in panel (a) and two-component quasiequilibrium in panel (b). In each case the carrier distribution is a Fermi function in each band (with both bands adding a contribution to the Drude weight) with a temperature that is varied to span all ratios with the chemical potential. First, for equilibrium, panel (a) shows that the scaled curves are largely insensitive to the balance between chemical potential and temperature with all curves overlapping. For frequencies on the order of half the Drude weight or smaller ($\omega \lesssim \omega_{\rm D}/2$), the dispersion curves overlap with the square-root Drude dispersion predicted by the local model. Outside this frequency range, the curves each follow the zero-temperature equilibrium solution (red curve). Even in the high-temperature limit, $T \gg \mu$ ($\mu/T = 0$, black curve), the dispersion is not significantly different from the zero-temperature result. Due to the similarity of these curves, they may all be approximated by a single function, e.g.,

$$\frac{\omega_{\rm pl}(q)}{\omega_{\rm D}} = \ln\left(\frac{e^{\kappa(1+e^{a\kappa})\sqrt{2\alpha_{\rm g}\tilde{q}}} + e^{\kappa(a+b\tilde{q})}}{1 + e^{a\kappa}}\right)/\kappa, \tag{24}$$

which asymptotically approaches the Drude dispersion for $q \to 0$ and approaches a straight line at other values, where κ,a,b are parameters to be fitted (with values $\kappa = -2.79$, $a = 1.06$, $b = 0.45$ for suspended graphene).

The imaginary part of the complex frequency solution, i.e., the loss curve, does vary with temperature. This can be seen in the right panel of Fig. 5(a) where the red curve, representing zero temperature, has frequencies where there is no loss, i.e., where the plasmon dispersion passes through the loss-free region. When the temperature rises, absorption processes that would be loss free at zero temperature are now no longer Pauli blocked and their rates become finite, resulting in loss in the plasmon dispersion. The extremal curve of the high-temperature limit has a finite loss, and all intermediate curves are bounded by the high- and zero-temperature limits.

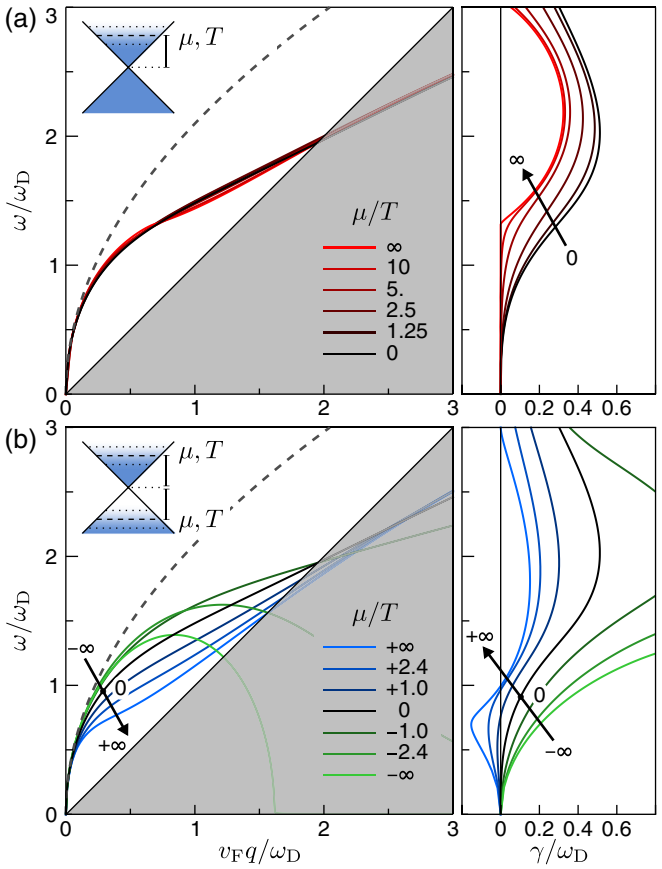

FIG. 5. Plasmon dispersion curves at finite temperature for (a) equilibrium graphene and (b) two-component quasiequilibrium. All curves are scaled to the Drude weight, ω_D, and plotted alongside the local Drude limit (dashed line). The curves progress from zero temperature [red in (a), blue in (b)], towards the case where temperature dominates over chemical potential [black curve, which is identical in (a) and (b)]. For the two-component case, (b), the curves continue for negative chemical potentials, i.e., for small probabilities of carriers in each band. Alongside the dispersion curves, scaled plasmon losses are plotted against frequency (right column).

In panel (b) of Fig. 5, plasmon dispersion curves are drawn for two-component quasiequilibrium. Here both positive and negative chemical potentials are solved for. Whereas in the equilibrium case, with a single Fermi level, a positive or negative chemical potential determines whether the Fermi level is found in the conduction or valence band, for a two-component quasiequilibrium, each band has its own distribution and Fermi level, and a positive chemical potential places the Fermi level within its band, and a negative outside of it. Particularly a negative chemical potential indicates a low density of carriers, i.e., at the end of the Fermi distribution tail, where the occupation probability for any state is less than one-half. Such distributions occur early in photoexcitation, when an excitation pulse thermalizes and there are relatively few carriers but these carriers have a large energy density.

In contrast to panel (a), Fig. 5(b) shows that the plasmon dispersion curves will spread out for different ratios of temperature to chemical potential. Each still follows the Drude square-root behavior for $\omega \lesssim \omega_D/2$, but the curves fan out after this. The black curve that represents temperature-dominated behavior ($\mu/T \to 0$) is the same curve as in the equilibrium case, as in both cases the Fermi level of each band is at the Dirac point. From here, curves with a positive chemical potential fall underneath, while curves with a negative chemical potential start to steepen over the high-temperature curve. For sufficiently negative μ, local extrema appear in the dispersion, where the group velocity, $\frac{\partial\omega}{\partial q}$, is zero; these are known as stopped-light points [34,35]. The extremal curve ($\mu/T \to -\infty$) has an analytic solution, solved for in Appendix B. The loss curves show that for curves with a positive chemical potential, there are frequencies ($\hbar\omega < 2\mu$) where the loss is negative; i.e., there is gain. As explained in the previous section, this is where the rate of stimulated emission processes is greater than absorption processes. In the high-temperature limit and for negative chemical potentials, the bands never have an occupancy probability greater than one-half, resulting in greater rates of plasmon absorption than emission at all frequencies. For low carrier numbers ($\mu < 0$), the carriers in the system allow plasmons to be supported, but these plasmons are far more likely to be absorbed than to stimulate emission, and hence show the highest loss rates in the figure.

This section has shown that the shape of plasmon dispersion curves, once scaled to the Drude weight, is approximately constant for equilibrium graphene, but can vary quantitatively and qualitatively for nonequilibrium carrier distributions such as a two-component quasiequilibrium, especially for configurations where there is a low density of high-energy carriers in the system. Carrier inversion and high temperatures contribute to the gain and loss channels of the plasmons such that the low-loss approximation, $|\mathrm{Im}\,\omega| \ll \mathrm{Re}\,\omega$, is no longer valid, and that plasmon dispersion and losses should be calculated using this nonequilibrium complex-frequency procedure. In the next section, we show how the nonequilibrium carrier distributions produced immediately following photoexcitation can further affect the polarization and plasmons.

IV. PHOTOEXCITATION NONEQUILIBRIUM

Until now, only polarization functions derived from Fermi distributions have been shown. The method presented in Sec. II generalizes to calculations with arbitrary carrier occupations. We present a model for photoexcitation which describes a hot-carrier nonequilibrium model. That is, a transient population of photoexcited electrons are modeled to be placed above a bath of thermalized quasiequilibrium carriers.

The photoexcited carriers are modeled with a hyperbolic secant (sech) profile [36], above a background of relaxed quasiequilibrium carriers. Both conduction and valence bands have the distribution

$$n_{e/h}(\epsilon) = \frac{1}{1+\exp(\frac{\epsilon-\mu}{T})} + n_{s0}\,\mathrm{sech}\left(\frac{\epsilon-\epsilon_s}{\gamma_s}\right). \tag{25}$$

The extra parameters introduced here are the excitation energy ϵ_s (which is half the pump photon energy), the population width γ_s (which relates to the pump width and ratio of pump rate to electron recombination rate), and the peak occupation n_{s0}, which ranges from 0 for no pump to 0.5 at transparency. Calculating the complex contour integral of the sech contribution is almost identical to that of the Fermi distribution; like

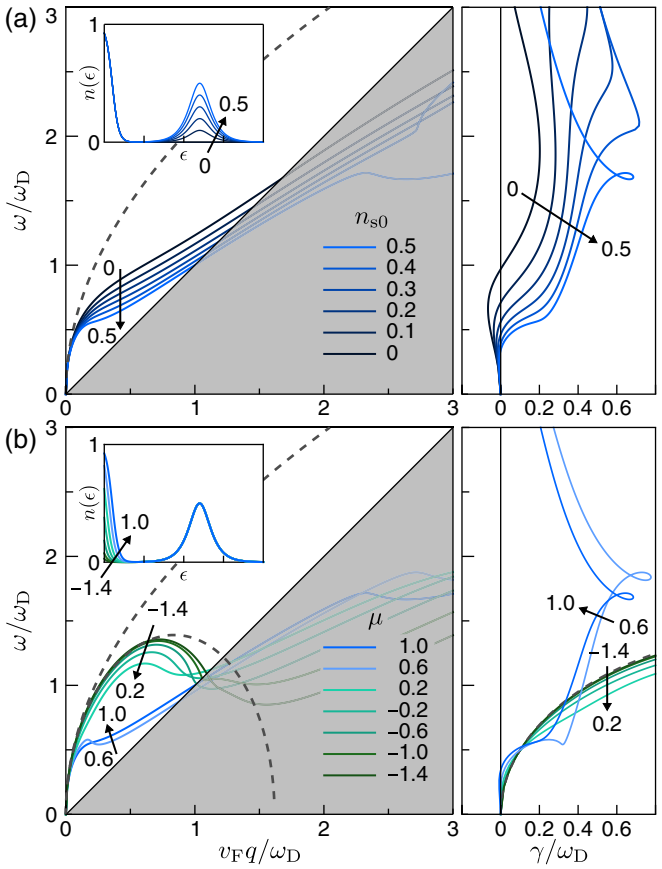

FIG. 6. Plasmon dispersion curves of photoexcited graphene with a carrier distribution function of a sech excitation profile above the thermalized Fermi bath, with parameters $\mu_e = \mu_h$, $T = 0.4$ eV, $\epsilon_s = 1.2$ eV, $\gamma_s = 0.12$ eV. In panel (a), the bath chemical potential is set at $\mu_e = 0.1$ eV and the peak excitation occupation, n_{s0}, varies in the range [0,0.5] between no excitation and transparency. In panel (b) μ_e varies in the range [−1.4,1.0] with n_{s0} fixed at 0.5. The carrier distribution function is inset in each part, and the plasmon loss plotted in the rightmost panels. All curves are scaled to the Drude weight, ω_D.

the Fermi distribution, the sech distribution has evenly spaced poles at Matsubara frequencies, $\epsilon^{(n)} = \epsilon_s + i(2n+1)\pi\gamma_s/2$ with residue $-i(-1)^n n_{s0}\gamma_s/2$; therefore the same algorithm is employed.

Plasmon dispersion curves are shown for a photoexcited carrier distribution function in Fig. 6. In panel (a) the height of the sech peak is varied from 0.5 (i.e., transparency) to 0 (no excitation). The parameters, given in the figure caption, are such that when the sech peak is at its maximum height ($n_{s0} = 0.5$), it contributes approximately twice as much to the Drude weight as the Fermi bath does. This contribution decreases linearly to zero as the height of the sech peak is lowered. The dispersion curves produced for each height of the sech distribution follow the Drude dispersion in the local limit and then spread out for higher wave vectors, being pushed down as n_{s0} increases. This is in a manner similar to that when temperature is increased in the quasiequilibrium case. The loss of the plasmon dispersion curves increases with the height of the sech peak, which is perhaps unexpected since in principal more carrier inversion is being added to the system; however until these carriers relax within the band, there are not enough emission channels at any particular energy to compete with absorption and have a net gain for plasmons. A more stark change comes in panel (b) when n_{s0} is held constant at 0.5, and instead, the chemical potential of the thermalized bath is reduced. The curves split into two bundles, with those with the smallest chemical potentials attracted towards the low density-high energy limit, as in quasiequilibrium for $\mu/T \to -\infty$ in Sec. III B and Appendix B. In this case points of zero group velocity (turning points) appear in the dispersion, and the dispersion is significantly different from that solved for equilibrium graphene.

This section has shown that immediately after photoexcitation, while the carriers relax initially to a two-component quasiequilibrium, the momentary plasmon dispersion and screening function can be qualitatively different. Particularly, excited carriers need to relax within their band before they contribute to plasmon gain processes. The sech distribution has been used here to model photoexcitation; however a sum of one or more sech functions may be used to fit other carrier distributions, such as the nonthermal carriers observed during relaxation in Ref. [37].

V. CONCLUSION

This work has outlined the procedure for efficiently evaluating RPA polarization functions and plasmon dispersion relations in monolayer graphene for arbitrary nonequilibrium carrier occupations. This has allowed for these quantities to be calculated in cases of high temperature, both in equilibrium and a two-component plasma quasiequilibrium, as well as in application to a model for carriers immediately following photoexcitation, where they are momentarily excited to a ring of high-energy states. The nonequilibrium carrier occupations explored in this paper are transient and will evolve through a range of configurations as the system relaxes. The irreducible polarization function, calculated here, is a key quantity of the dynamic screening, which influences all carrier-carrier interactions, such as Auger recombination and others which may play a role in carrier relaxation in graphene [37,38]. The theory is general and can be modified to describe graphene outside of the Dirac cone regime [25,39,40], and indeed may be applied to other two-dimensional materials [41] such as transition-metal dichalcogenides.

ACKNOWLEDGMENT

The authors acknowledge financial support provided by the Engineering and Physical Sciences Research Council (United Kingdom).

APPENDIX A: BRANCH CUTS

To manage the branches of the kernel functions [Eq. (10a)], a choice of branch cuts must be defined that anchors to the branch points. Figure 7 shows a set of choices that have been used in this paper. Broadly, the choices available are closed or open branch cuts. Closed cuts connect two branch points together and are finite in extent, whereas open branch cuts start

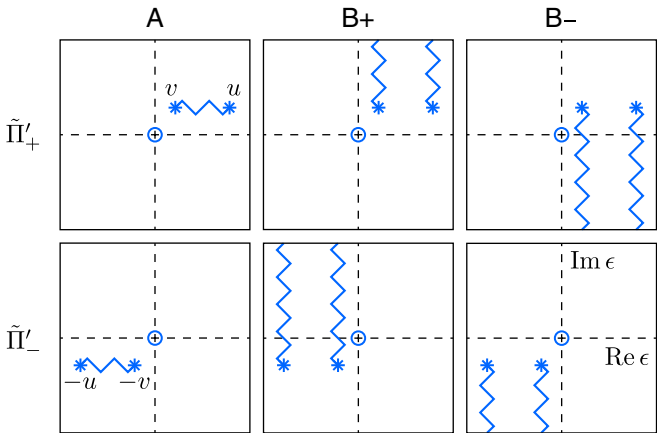

FIG. 7. Options for the position of branch cuts in the kernel function. The top row is for the $\tilde{\Pi}'_+$ function, which has branch points at u and v, while the bottom row is for $\tilde{\Pi}'_-$, where the branch points are at $-u$ and $-v$. The columns represent choices for the branch cuts. A is a closed cut $[u,v]$ or $[-u,-v]$, where B± are open cuts such as $[u,\pm i\infty)$, etc., with their branch cuts starting from the branch point and extending to infinity. The circle at the origin of each diagram represents a zero of the function. On the principal branch of the kernels, $\tilde{\Pi}'_\pm(\epsilon=0)=0$.

from one branch point and continue to infinity. In the figure, these are labeled A for the closed cuts and B± for open cuts with their end point at $\pm i\infty$. In the paper, it was beneficial to use B+ and B− (for $\tilde{\Pi}'_+$ and $\tilde{\Pi}'_-$, respectively) in Sec. II A when evaluating the polarization function, and to use A and B+ in Sec. II B when solving for plasmons.

Most computer implementations of the complex square root, $\sqrt{z}$, place the branch cut on the negative real axis, choosing the branch with positive real part. The square root can be replaced with $\sqrt{z}\to e^{i\theta/2}\sqrt{e^{-i\theta}z}$, which rotates the branch cut counterclockwise by θ from 0 to 4π, i.e., two full turns. The other branch can always be accessed by multiplying the square root by -1, i.e., $\sqrt{z}\to-\sqrt{z}$. This can be used to construct kernel functions with different branch cut choices.

The A form is the simplest, and will be used as a starting point,

$$\mathsf{A}:\ \tilde{\Pi}'_+(\epsilon)=\frac{-2\sqrt{\epsilon-u}\sqrt{\epsilon-v}+2\epsilon}{\sqrt{u}\sqrt{v}}-2, \quad \text{(A1a)}$$

$$\mathsf{A}:\ \tilde{\Pi}'_-(\epsilon)=\frac{-2\sqrt{\epsilon+u}\sqrt{\epsilon+v}-2\epsilon}{\sqrt{u}\sqrt{v}}-2. \quad \text{(A1b)}$$

Individually, the square roots $\sqrt{\epsilon-u}$, $\sqrt{\epsilon-v}$ have a branch point at u or v and their cuts extend to $\epsilon\to-\infty$. In combination the two square-root branches cancel as they overlap leaving a branch cut between u and v. In order to calculate the B forms, these branch cuts are rotated by $\pi/2$ clockwise for B+ and counterclockwise for B−. The principal branch is selected, by ensuring a root at zero for $\mathrm{Im}\,u=\mathrm{Im}\,v>0$, which yields the following as the B forms:

$$\mathsf{B}+:\ \tilde{\Pi}'_+(\epsilon)=\frac{2i\sqrt{i(\epsilon-u)}\sqrt{i(\epsilon-v)}+2\epsilon}{\sqrt{u}\sqrt{v}}-2, \quad \text{(A2a)}$$

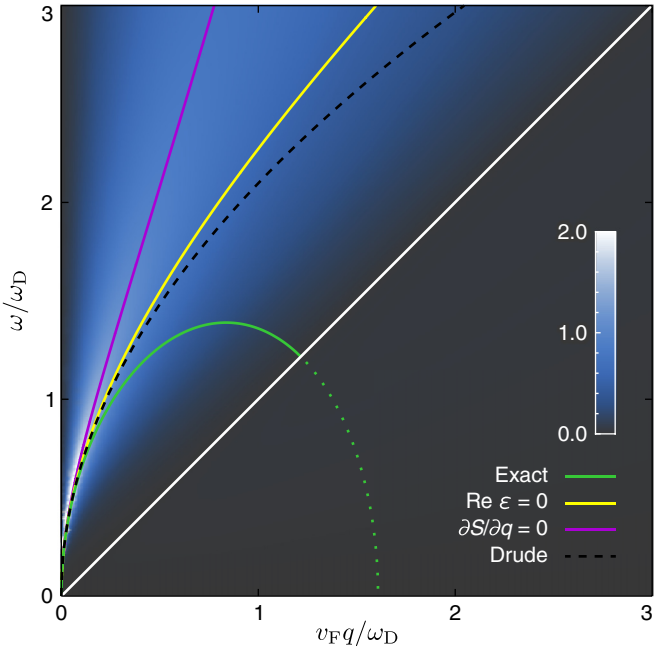

FIG. 8. Energy-loss function, $S=-\mathrm{Im}\,\varepsilon(q,\omega)^{-1}$, for graphene in the highly energetic limit. Overlaid are the analytic plasmon solution (green), solved for in this section, alongside a number of approximations, i.e., the low-loss approximation, $\mathrm{Re}\,\varepsilon=0$ (yellow), following the peak of the loss function (magenta) and the local Drude model (black dashed).

$$\mathsf{B}+:\ \tilde{\Pi}'_-(\epsilon)=\frac{-2i\sqrt{i(\epsilon+u)}\sqrt{i(\epsilon+v)}-2\epsilon}{\sqrt{u}\sqrt{v}}-2, \quad \text{(A2b)}$$

$$\mathsf{B}-:\ \tilde{\Pi}'_+(\epsilon)=\frac{-2i\sqrt{-i(\epsilon-u)}\sqrt{-i(\epsilon-v)}+2\epsilon}{\sqrt{u}\sqrt{v}}-2, \quad \text{(A2c)}$$

$$\mathsf{B}-:\ \tilde{\Pi}'_-(\epsilon)=\frac{2i\sqrt{-i(\epsilon+u)}\sqrt{-i(\epsilon+v)}-2\epsilon}{\sqrt{u}\sqrt{v}}-2. \quad \text{(A2d)}$$

As a final note, strictly speaking, the $\pm2\epsilon/\sqrt{u}\sqrt{v}$ terms are superfluous as they cancel out. They are included for numerical stability, such that each form limits to a constant rather than growing linearly; this assists in the convergence of numerical integrations.

APPENDIX B: HIGHLY ENERGETIC LIMIT SOLUTION

In Figs. 5 and 6, the plasmon dispersion curves that corresponded to a small number of high-energy carriers in the system were shown to have turning points and curve downwards in an ellipse-like manner. In the limiting case, this plasmon dispersion curve has an analytic solution, shown in Fig. 8, which is worth examining because it is demonstrably different to the approximations often used to describe plasmons in the system, i.e., taking the low-loss approximation that would solve $\mathrm{Re}\,\varepsilon(q,\mathrm{Re}\,\omega)=0$ for a real frequency and taking a Taylor expansion for the imaginary part, or alternatively by tracing where the peaks are in the energy-loss function.

To start we assume a delta-function occupation,

$$n(\epsilon) = \hbar\omega_{\mathrm{D}}\delta(\epsilon - \epsilon_0). \tag{B1}$$

On face value, this would seem problematic since the occupation probability is above 1; however, this can be seen as an approximation function such as a sech or a Gaussian with a sharp peak. Putting this through Eq. (8), and taking the limit, either as $\omega_{\mathrm{D}} \to 0$ or equivalently $\epsilon_0 \to \infty$, i.e., $\hbar\omega_{\mathrm{D}} \ll \epsilon_0$, representing a small population of highly energetic carriers, the dielectric function becomes

$$\varepsilon(q,\omega) = 1 + \frac{\alpha_{\mathrm{g}}}{\tilde{q}}\left(\frac{i\pi\tilde{q}^2 - 8\tilde{\omega}}{2\sqrt{\tilde{\omega}+\tilde{q}}\sqrt{\tilde{\omega}-\tilde{q}}} + 4\right), \tag{B2}$$

in terms of the scaled coordinates, $(\tilde{q},\tilde{\omega})$, introduced in Sec. III B. The complex zeros of this function can be solved for, returning the closed form expression for the complex frequency plasmon dispersion,

$$\tilde{\omega} = \frac{(4\alpha_{\mathrm{g}}+\tilde{q})\sqrt{8\alpha_{\mathrm{g}}\tilde{q} - \left[\left(\frac{\pi\alpha_{\mathrm{g}}}{2}\right)^2 - 1\right]\tilde{q}^2}}{8\alpha_{\mathrm{g}}+\tilde{q}} - i\frac{2\pi\alpha_{\mathrm{g}}^2\tilde{q}}{8\alpha_{\mathrm{g}}+\tilde{q}}, \tag{B3}$$

which reproduces the Drude limit, $\tilde{\omega} = \sqrt{2\alpha_{\mathrm{g}}\tilde{q}} - i\pi\alpha_{\mathrm{g}}\tilde{q}/4$, as $\tilde{q} \to 0$.

This curve, shown in green in Fig. 8, is an attractor for carrier systems that are dominated by high-energy excitations, such as the two-component plasma when $-\mu \gg T$, or when carriers are photoexcited in an otherwise empty band.

[1] G. F. Giuliani and J. J. Quinn, Lifetime of a quasiparticle in a two-dimensional electron gas, Phys. Rev. B **26**, 4421 (1982).

[2] A. Bostwick, T. Ohta, T. Seyller, K. Horn, and E. Rotenberg, Quasiparticle dynamics in graphene, Nat. Phys. **3**, 36 (2007).

[3] J. C. W. Song and L. S. Levitov, Energy flows in graphene: Hot carrier dynamics and cooling, J. Phys.: Condens. Matter **27**, 164201 (2015).

[4] J. M. Dawlaty, S. Shivaraman, M. Chandrashekhar, F. Rana, and M. G. Spencer, Measurement of ultrafast carrier dynamics in epitaxial graphene, Appl. Phys. Lett. **92**, 042116 (2008).

[5] T. Li, L. Luo, M. Hupalo, J. Zhang, M. C. Tringides, J. Schmalian, and J. Wang, Femtosecond Population Inversion and Stimulated Emission of Dense Dirac Fermions in Graphene, Phys. Rev. Lett. **108**, 167401 (2012).

[6] J. Zhang, J. Schmalian, T. Li, and J. Wang, Transient charge and energy balance in graphene induced by ultrafast photoexcitation, J. Phys.: Condens. Matter **25**, 314201 (2013).

[7] F. Meng, M. D. Thomson, F. Bianco, A. Rossi, D. Convertino, A. Tredicucci, C. Coletti, and H. G. Roskos, Saturable absorption of femtosecond optical pulses in multilayer turbostratic graphene, Opt. Express **24**, 15261 (2016).

[8] S. Butscher, F. Milde, M. Hirtschulz, E. Malić, and A. Knorr, Hot electron relaxation and phonon dynamics in graphene, Appl. Phys. Lett. **91**, 203103 (2007).

[9] F. Rana, P. A. George, J. H. Strait, J. M. Dawlaty, S. Shivaraman, M. Chandrashekhar, and M. G. Spencer, Carrier recombination and generation rates for intravalley and intervalley phonon scattering in graphene, Phys. Rev. B **79**, 115447 (2009).

[10] H. Wang, J. H. Strait, P. A. George, S. Shivaraman, V. B. Shields, M. Chandrashekhar, J. Hwang, F. Rana, M. G. Spencer, C. S. Ruiz-Vargas, and J. Park, Ultrafast relaxation dynamics of hot optical phonons in graphene, Appl. Phys. Lett. **96**, 081917 (2010).

[11] A. Tomadin, D. Brida, G. Cerullo, A. C. Ferrari, and M. Polini, Nonequilibrium dynamics of photoexcited electrons in graphene: Collinear scattering, Auger processes, and the impact of screening, Phys. Rev. B **88**, 035430 (2013).

[12] P. F. Maldague, Many-body corrections to the polarizability of the two-dimensional electron gas, Surf. Sci. **73**, 296 (1978).

[13] B. Van Duppen, A. Tomadin, A. N. Grigorenko, and M. Polini, Current-induced birefringent absorption and non-reciprocal plasmons in graphene, 2D Mater. **3**, 15011 (2016).

[14] X. G. Ni, L. Wang, M. D. Goldflam, M. Wagner, Z. Fei, A. S. McLeod, M. K. Liu, F. Keilmann, B. Özyilmaz, A. H. Castro Neto, J. Hone, M. M. Fogler, and D. N. Basov, Ultrafast optical switching of infrared plasmon polaritons in high-mobility graphene, Nat. Photonics **10**, 244 (2016).

[15] A. J. Chaves, N. M. R. Peres, and T. Low, Pumping electrons in graphene to the M point in the Brillouin zone: Emergence of anisotropic plasmons, Phys. Rev. B **94**, 195438 (2016).

[16] A. F. Page, F. Ballout, O. Hess, and J. M. Hamm, Nonequilibrium plasmons with gain in graphene, Phys. Rev. B **91**, 075404 (2015).

[17] J. M. Hamm, A. F. Page, J. Bravo-Abad, F. J. Garcia-Vidal, and O. Hess, Nonequilibrium plasmon emission drives ultrafast carrier relaxation dynamics in photoexcited graphene, Phys. Rev. B **93**, 041408(R) (2016).

[18] G. Giuliani and G. Vignale, *Quantum Theory of the Electron Liquid* (Cambridge University Press, Cambridge, 2005).

[19] J. Hofmann, E. Barnes, and S. Das Sarma, Why Does Graphene Behave as a Weakly Interacting System?, Phys. Rev. Lett. **113**, 105502 (2014).

[20] B. Wunsch, T. Stauber, F. Sols, and F. Guinea, Dynamical polarization of graphene at finite doping, New J. Phys. **8**, 318 (2006).

[21] E. H. Hwang and S. Das Sarma, Dielectric function, screening, and plasmons in two-dimensional graphene, Phys. Rev. B **75**, 205418 (2007).

[22] L. P. Kadanoff, G. Baym, and D. Pines, *Quantum Statistical Mechanics*, Advanced Books Classics Series (Perseus Books, New York, 1994).

[23] F. T. Vasko and O. E. Raichev, *Quantum Kinetic Theory and Applications: Electrons, Photons, Phonons* (Springer, New York, 2005).

[24] P. A. George, J. H. Strait, J. M. Dawlaty, S. Shivaraman, M. Chandrashekhar, F. Rana, and M. G. Spencer, Ultrafast optical-pump terahertz-probe spectroscopy of the carrier relaxation and recombination dynamics in epitaxial graphene, Nano Lett. **8**, 4248 (2008).

[25] P. K. Pyatkovskiy, Dynamical polarization, screening, and plasmons in gapped graphene, J. Phys.: Condens. Matter **21**, 025506 (2009).

[26] S. M. Kukhtaruk and V. A. Kochelap, Semiclassical analysis of intraband collective excitations in a two-dimensional electron gas with Dirac spectrum, Phys. Rev. B **92**, 041409(R) (2015).
[27] D. V. Khveshchenko, Coulomb-interacting Dirac fermions in disordered graphene, Phys. Rev. B **74**, 161402 (2006).
[28] X.-F. Wang and T. Chakraborty, Collective excitations of Dirac electrons in a graphene layer with spin-orbit interactions, Phys. Rev. B **75**, 033408 (2007).
[29] M. R. Ramezanali, M. M. Vazifeh, R. Asgari, M. Polini, and A. H. MacDonald, Finite-temperature screening and the specific heat of doped graphene sheets, J. Phys. A **42**, 214015 (2009).
[30] O. Vafek, Thermoplasma Polariton within Scaling Theory of Single-Layer Graphene, Phys. Rev. Lett. **97**, 266406 (2006).
[31] L. A. Falkovsky and A. A. Varlamov, Space-time dispersion of graphene conductivity, Eur. Phys. J. B **56**, 281 (2007).
[32] S. H. Abedinpour, G. Vignale, A. Principi, M. Polini, W.-K. Tse, and A. H. MacDonald, Drude weight, plasmon dispersion, and ac conductivity in doped graphene sheets, Phys. Rev. B **84**, 045429 (2011).
[33] L. A. Falkovsky and S. S. Pershoguba, Optical far-infrared properties of a graphene monolayer and multilayer, Phys. Rev. B **76**, 153410 (2007).
[34] K. L. Tsakmakidis, T. W. Pickering, J. M. Hamm, A. F. Page, and O. Hess, Completely Stopped and Dispersionless Light in Plasmonic Waveguides, Phys. Rev. Lett. **112**, 167401 (2014).
[35] T. W. Pickering, J. M. Hamm, A. F. Page, S. Wuestner, and O. Hess, Cavity-free plasmonic nanolasing enabled by dispersionless stopped light, Nat. Commun. **5**, 4972 (2014).
[36] W. W. Chow and S. W. Koch, *Semiconductor-Laser Fundamentals: Physics of the Gain Materials* (Springer, Berlin, 2013).
[37] I. Gierz, F. Calegari, S. Aeschlimann, M. C. Cervantes, C. Cacho, R. T. Chapman, E. Springate, S. Link, U. Starke, C. R. Ast, and A. Cavalleri, Tracking Primary Thermalization Events in Graphene with Photoemission at Extreme Time Scales, Phys. Rev. Lett. **115**, 086803 (2015).
[38] D. Giovanni, G. Yu, G. Xing, M. L. Leek, and T. C. Sum, Measurement of sub-10 fs Auger processes in monolayer graphene, Opt. Express **23**, 21107 (2015).
[39] A. Hill, S. A. Mikhailov, and K. Ziegler, Dielectric function and plasmons in graphene, Europhys. Lett. **87**, 27005 (2009).
[40] M. T. Mihnev, F. Wang, G. Liu, S. Rothwell, P. I. Cohen, L. C. Feldman, E. H. Conrad, and T. B. Norris, Evidence for bandgap opening in buckled epitaxial graphene from ultrafast time-resolved terahertz spectroscopy, Appl. Phys. Lett. **107**, 173107 (2015).
[41] R. Roldan, L. Chirolli, E. Prada, J. A. Silva-Guillen, P. San-Jose, and F. Guinea, Theory of 2D crystals: Graphene and beyond, Chem. Soc. Rev. **46**, 4387 (2017).